## Laser surface remelting of Al-Mg and Al-Si-Mg alloys: microstructure and properties

Danusa Araújo de Moura <sup>1</sup> © Anderson Thadeu Nunes <sup>1</sup> © José Eduardo Spinelli <sup>1\*</sup> ®

#### Abstract

Solidification is one of the most widely used manufacturing processes for metallic components. In the context of surface treatments, localized melting and resolidification represent an important application that deserves special attention. Among these, the Laser Surface Remelting (LSR) process is notable for creating a thin molten layer on the alloy surface. This occurs through the application of a continuous high-energy-density laser beam. Once the laser is removed, rapid solidification of the molten region is achieved by heat extraction into the remaining cold part of the material (the substrate), which has a much larger mass. Currently, there is great interest in new aluminum (Al) and magnesium (Mg) alloys for lightweight components such as pistons, manifolds, reducers, oil pans, and chassis, as well as in their laser treatments. Although LSR of Al-Cu alloys is well understood, there is a gap in studies on AlSi10Mg and Al-Mg alloys, which have high application potential. This short review addresses LSR applied to these less-explored alloys. Methods for determining cooling rates and their correlation with the resulting laser-modified microstructures will be presented. This study investigates the influence of laser surface remelting on the microstructure and mechanical properties of Al-Si10MgNi and Al-Mg-Sc alloys. The aim is to understand how alloy composition and laser parameters affect solidification features and their correlation with nanohardness and wear behavior. The results indicate that increasing Ni content (from 1Ni to 3Ni) in Al-Si10Mg alloys refines the microstructure and develops a third phase (Al<sub>3</sub>Ni), which increases the hardness. In Al-Mg-Sc alloys, higher Mg levels and slower scanning speeds promote cellular coarsening and affect hardness distribution across the laser melt pool.

Keywords: Laser surface remelting; Solidification; Microstructures; Al alloys.

### 1 Introduction

Aluminum (Al) boasts excellent properties such as machinability, ductility, weldability, and ease of recycling. However, Al alloys can be unsuitable for certain applications due to insufficient resistance to corrosion, erosion, fatigue, and wear. Surface modification, without degrading the core, is considered a viable solution [1,2].

Laser-based surface engineering is a promising alternative for surface modification. This non-contact technique demonstrates potential for innovations in materials. Research interest has grown significantly since 2010 [3,4] allowing for the development of new microstructures due to rapid solidification [5].

Laser surface modifications are categorized into five main types: (i) laser surface remelting (LSR); (ii) laser surface alloying; (iii) laser surface composite; (iv) laser cladding; and (v) laser shock peening. All categories, apart from laser shock peening, involve the melting of the substrate, with or without the addition of material. These processes require

shielding gas to prevent oxidation and crack stabilizers (except for LSR). Moreover, the choice of process depends on the desired properties [6,7]. Laser applications are industrially competitive due to their cleanliness, high speed, and automation. Kannatey-Asibu [8] describes the principles of laser processing, including types such as Nd:YAG, CO<sub>2</sub>, diode, and free-electron lasers.

LSR occurs without the addition of elements, with the surface being subjected only to laser radiation. It is an emerging process characterized by rapid melting and cooling, offering versatility in rapid solidification, controlled by power and scanning speed. Both parameters influence both heating and cooling [9,10]. The intensity (I) is given by the relationship between the power (P) and the laser beam radius  $(\omega)$ : I = P/ $(\pi^*\omega^2)$  [8].

LSR generates a thin remelted region. This region is self-cooled by the substrate, which results in rapid solidification and microstructural changes [8], with cooling rates ranging from  $10^4$  to  $10^8$  K/s [11].

E-mails: atnthadeu@yahoo.com.br; danusa@ufscar.br



2176-1523 © 2025. Moura et al. Published by ABM. This is an Open Access article distributed under the terms of the Creative Commons Attribution license (https://creativecommons.org/licenses/by/4.0/), which permits unrestricted use, distribution, and reproduction in any medium, provided the original work is properly cited.

<sup>&</sup>lt;sup>1</sup>Programa de pós-graduação em Ciência e Engenharia de Materiais, Departamento de Engenharia de Materiais, Universidade Federal de São Carlos – UFSCar, São Carlos, SP, Brasil.

<sup>\*</sup>Corresponding author: spinelli@ufscar.br

### 1.1 Aim of this short review

Analyses of studies on LSR in Al alloys have revealed gaps in the development of microstructures and process control. This short review presents recent research conducted by the M2PS group (http://www.m2ps.ufscar.br) at UFSCar, Brazil on laser surface remelting (LSR) of Al-Si10Mg and Al-Mg-Sc alloys, materials with growing industrial relevance but still underexplored in terms of rapid solidification behavior and laser remelting treatments. This study aims to estimate the cooling rate in Al-Si10MgNi alloys (with 0 to 3 wt.% Ni) to correlate dendritic spacing within the molten pool with cooling conditions, and to assess the effects of microstructural refinement on nanohardness and wear, as well as the influence of Ni addition on these properties. Additionally, for the Al-(3, 5, 10)wt.%Mg-0.1wt.%Sc alloys, the objective is to investigate the evolution of cellular spacing and band formation in the molten pool as a function of Mg content and laser processing parameters (scanning speed and power), along with the evaluation of microhardness evolution under these varying conditions. The work aims to support advances in surface engineering of Al alloys used in critical lightweight applications.

### 2 Benefits of LSR and impacts on the microstructure of Al allovs

In addition to its use as a post-processing technique for additive manufacturing [12-14], LSR enhances microstructure and disintegrates surface precipitates, thereby increasing corrosion resistance. LSR reduces inter-particle spacing, refines grains, and distributes them homogeneously, which in turn increases hardness. It also decreases porosity and spalling, resulting in higher microhardness, surface uniformity, and wear resistance.

Additionally, LSR promotes beneficial residual surface compressive stress that improves fatigue resistance. These factors collectively extend the service life of laser-treated parts.

The characteristics of the remelted layer are influenced by the initial alloy composition, prior microstructure, and applied laser energy [15,16].

LSR is a promising technique for grain refinement and achieving microstructural uniformity with fine dendrites or cells in the surface layers of metallic alloys [17-19]. With the increasing use of aluminum alloys in automotive components like pistons, crankcases, and chassis—where lightness is essential to reduce weight and fuel consumption—there's a growing need for surface treatments, such as LSR, capable of modifying microstructural characteristics.

The interaction between the laser beam and the metallic surface depends on variables such as power density and residence time, which control the thermal regime and the resulting effects [20]. However, measuring critical parameters like temperature fields and solidification velocities remains

a challenge due to the small scale and rapid evolution of the process [21].

Studies demonstrate the benefits of LSR in Al-Si alloys. Tomida et al. [22] reported, in Al-20wt.%Si and Al-30wt.%Si alloys, a reduction of primary Si particles from 30  $\mu m$  to 3  $\mu m$  after CO $_2$  laser treatment, resulting in increased hardness and wear resistance—especially for the alloy with higher Si content. Osório et al. [23] observed microstructural refinement in Al-9wt.%Si alloy, with a reduction of secondary dendritic arm spacing to 2.5  $\mu m$  (compared to 15  $\mu m$  in the as-cast metal) and a consequent increase in hardness, although with a loss of corrosion resistance due to the increased grain boundary density.

High cooling rates are a characteristic feature of LSR. Roscher et al. [24] estimated  $6 \times 10^6$  K/s in laser-processed Al alloys, while Ramakrishnan et al. [10] consider any process with rates above  $10^2$  K/s as rapid solidification. These regimes promote grain refinement, increased solute solubility, and the formation of metastable phases, ultimately leading to higher microhardness.

Studies on laser remelting of Al alloys, particularly with Al-Cu alloys, reveal diverse morphologies: nanometric eutectics, degenerate eutectic structures, dendritic/cellular, banded structures, and supersaturated solid solutions. Gill et al. [25] noted that solidification velocities above 0.5 m/s replace the eutectic structure with bands of supersaturated  $\alpha$ -Al and  $\alpha$ -Al\_2Cu. Zimmerman et al. [26] indicate that high scanning speeds in Al-10wt.%Cu alloy form metastable phases and eutectic cells. Liu and Kang [27] reported that Al-Mg alloy is sensitive to the cooling rate, with an increase in eutectic fraction and a reduction in grain size as the cooling rate increases. Zhang et al. [28] observed that A356 alloy, treated by LSR, shows a significant increase in hardness and wear resistance due to microstructural refinement and solid solution strengthening.

New methodologies can be applied to analyze the properties, formed phases, and surface microstructures after LSR modification of Al alloys. In the case of the present review, the flowchart in Figure 1 shows a proposed combined or correlative analysis, taking into consideration different aspects of the same surface. Figure 1 illustrates the experimental approach adopted to analyze laser surface treatments. The procedure begins with the production of laser tracks by systematically varying the laser power (P) and scanning speed (V). These tracks are then evaluated for their geometric characteristics, followed by microstructural and morphological analysis using optical microscopy and SEM. Elemental composition is assessed through EDS. Subsequently, ImageJ software is used to quantify worn volume, and mechanical performance is evaluated via hardness and wear tests. Finally, a correlative analysis integrates all the results to establish relationships between processing parameters, microstructure, and mechanical behavior.

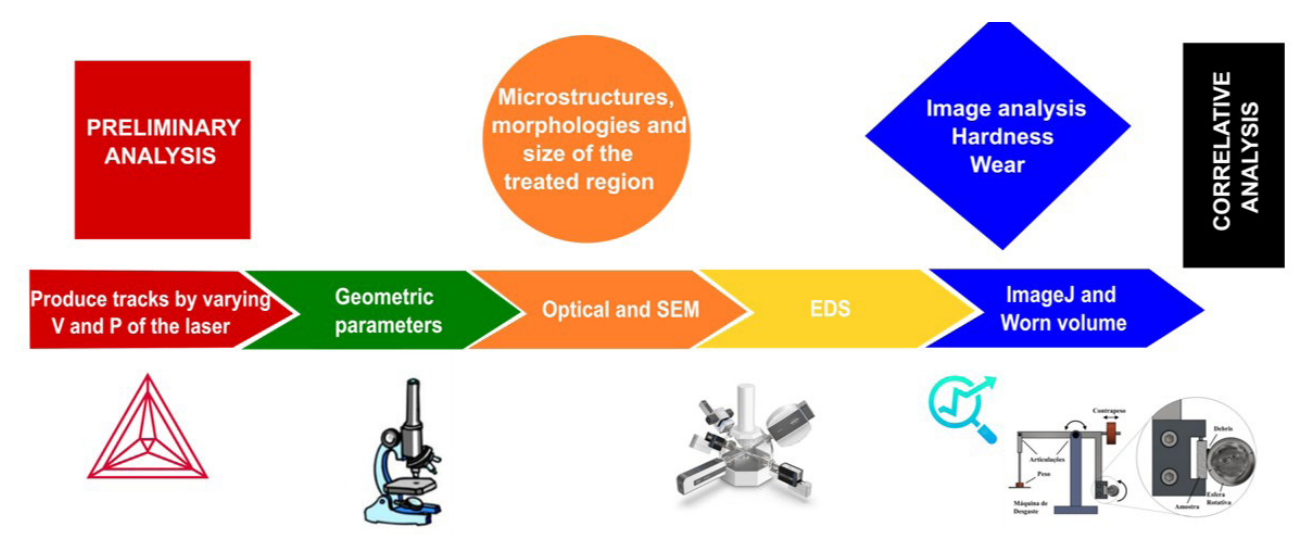


Figure 1. Experimental flowchart resulting in correlative and comprehensive analysis of surface aspects obtained by LSR.

## 3 Case study 1: cooling rate, microstructures, nanohardness, and wear in AlSi10MgNi(x) alloys

LSR treatments were applied to AlSi10Mg, AlSi10MgNi1, AlSi10MgNi2, AlSi10MgNi3 (wt.%) alloys using a 300 W CO<sub>2</sub> laser. Two conditions were tested: 300 W with 5 mm/s (400 J/mm<sup>2</sup>) and 300 W with 20 mm/s (100 J/mm<sup>2</sup>). The samples were surface-prepared by sanding and steel shot blasting to increase laser absorptivity [29]. The power of 300 W was selected as they represent the maximum output achievable by the equipment. Lower power levels were insufficient to remelt the alloy, and the same limitation was observed for scanning speeds above 20 mm/s. Microstructural analyses included Optical Microscopy (OM), Scanning Electron Microscopy with Energy Dispersive X-ray Spectroscopy (SEM/EDS), and X-ray Diffractometry (XRD) to identify phases. Microstructural spacings were measured by the intercept method, and the theoretical cooling rate was calculated using the Ashby and Easterling equation:  $\dot{T} = \frac{1}{4\left(\frac{Q}{Q}\right)} \left[30\right]$ , where A is the laser beam absorptivity

(0.18 as stated by Liu et al. [31]), v (m/s) is the laser beam scanning speed, Q (W) is the laser power, k (W/mK) is the thermal conductivity of the liquid determined via the CALPHAD method,  $T_0$  is the ambient temperature, and  $T_L$  is the *liquidus* temperature.

The micro-adhesive wear test utilized an AISI 52100 steel ball (25.4 mm) at 250 rpm, with a load of 0.5 N for 10 minutes. The worn volume (V) was calculated based on the cap diameter (d) and the sphere radius (R):  $v = \frac{\pi \cdot d^4}{64 \cdot R}$  [32]. Several load tests were conducted using the wear testing instrument to compare the wear volumes of laser-treated and as-cast samples. The results indicated sensitivity to the applied load, with the as-cast samples consistently exhibiting

significantly higher wear volumes. Based on these findings, a load of 0.5 N was selected for subsequent analyses.

High-speed nanoindentation tests were performed with a Hysitron TI980, using a Berkovich tip, trapezoidal loading (0.1 s load-hold-unload), and a peak load of 300μN.

Figure 2 illustrates the typical regions of laser-treated samples, both in cross-section (base, center, top) and longitudinal-section (surface).

On the surface of the laser-treated regions, cells also grew, characterizing a cellular/dendritic region. With increasing solidification velocity, the morphology of the solid/liquid (S/L) interface evolves in a sequence of planar, cellular, dendritic, high-velocity solidification cellular, and then back to planar [11,33]. Therefore, cells can form at both low and high velocities. At the top of the laser-treated region, a predominance of sectioned cells oriented in the transverse sections can be observed. In other words, the cells at the top changed their growth orientation relative to the base and began to grow in the same direction as the laser beam, as documented in other literature investigations [25,34-36]. Very fine cells are formed with a narrow range of 1.0  $\mu$ m to 2.0  $\mu$ m spacing.

Higher energy densities in the LSR result in larger dendritic spacings due to prolonged solidification times and microstructural coarsening. As shown in Figure 3, the microstructural spacing decreases from the base to the top of the melt pool. Higher Ni content ahead of the solid/liquid interface increases instability and refines spacing, while reduced diffusivity limits dendrite coarsening.

Given that thermal conductivity and liquidus temperature,  $T_L$ , varied minimally with the addition of Ni, the calculated cooling rates were similar for the studied alloys. For example, T was approximately  $1.3 \times 10^4$  K/s for samples processed at 400 J/mm² and  $5.0 \times 10^4$  K/s for those at 100 J/mm².

SEM images (Figure 4) revealed that, under both conditions, Silicon forms an irregular eutectic with fine and organized fibers, a result of rapid solidification [37,38]. Al3Ni, in turn, forms larger and more branched structures,

with a tendency towards plates [39-42]. Both phases appear to grow independently. Figure 4c exemplifies the phase segmentation to determine the experimental phase fraction along the melt pools.

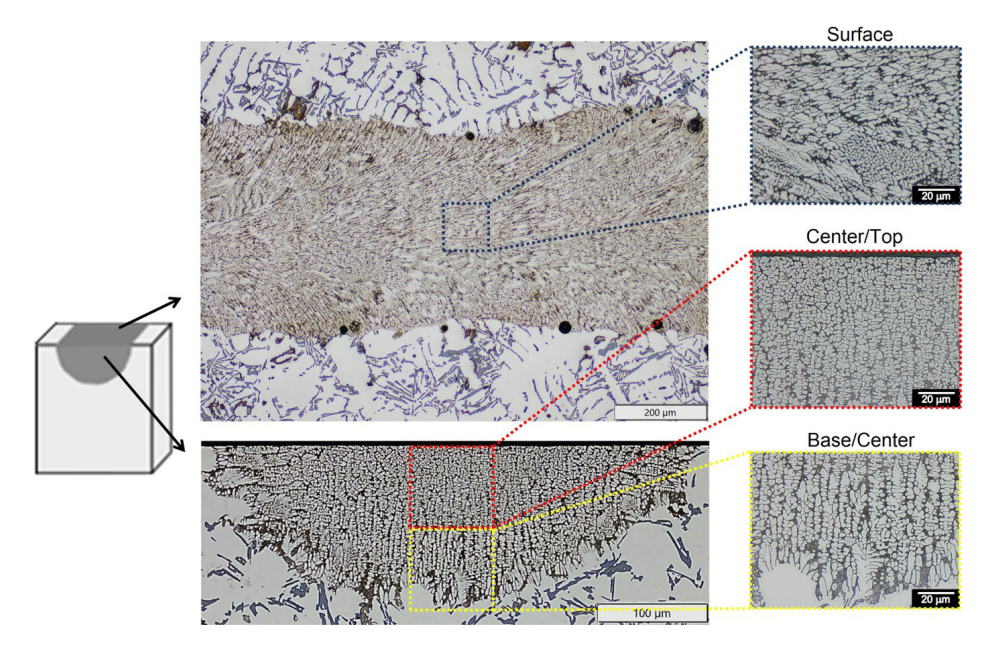


Figure 2. Scheme with optical microscopy images evidencing the laser-treated regions from laser surface remelting (LSR) of a AlSi10MgNi alloy.

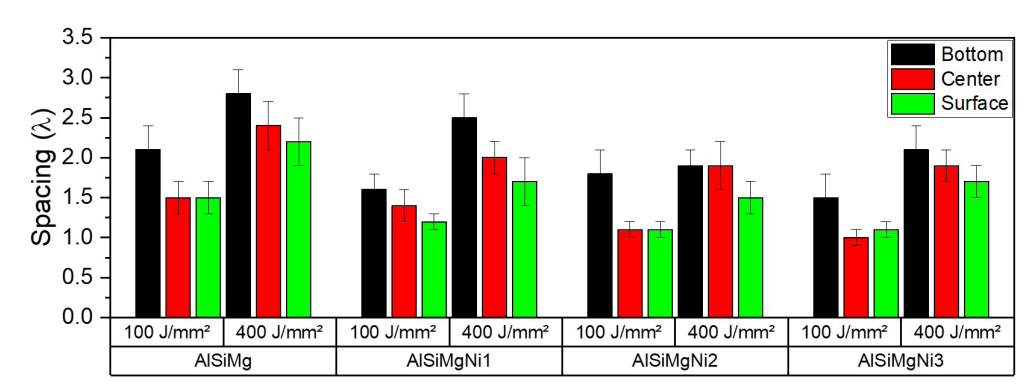
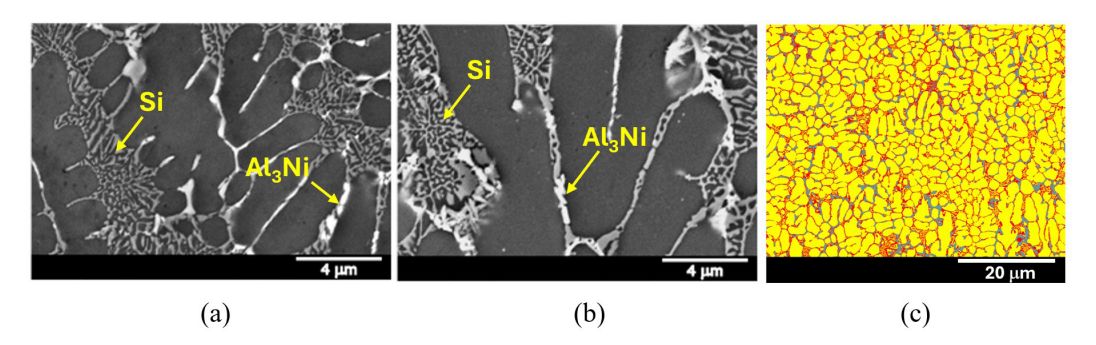


Figure 3. Secondary dendritic spacing for the base, center, and surface laser-treated regions in the AlSi10MgNi(x) alloys.



**Figure 4.** SEM images of laser remelted (LSR) AlSi10MgNi2 alloy samples processed at (a)  $100 \text{ J/mm}^2$ , (b)  $400 \text{ J/mm}^2$  and (c) segmentations of the phases present using Avizo 3D for the AlSi10MgNi2 alloy processed at  $400 \text{ J/mm}^2$ . Corresponding colors: yellow -  $\alpha$ -Al; red - Si; gray - Al<sub>3</sub>Ni.

EDS analysis (Figure 5) of the AlSi10MgNi3 alloy showed that Magnesium is uniformly distributed, while Nickel and Silicon are concentrated at the boundaries of the dendritic arms. This segregation is linked to their lower redistribution coefficients ( $k_0$ ) compared to Magnesium, which is less dense and distributes better within the remaining liquid [43-45].

The XRD patterns obtained for the alloys (Figure 6) confirmed the presence of  $\alpha$ -Al, Si, Mg2Si, and Al3Ni phases. A decrease in the intensity of the peaks corresponding to Si is also observed as the solidification speed, v, increases, with v corresponding to  $100 \text{ J/mm}^2 > 400 \text{ J/mm}^2$ . This likely occurred due to the high solidification rate, which results

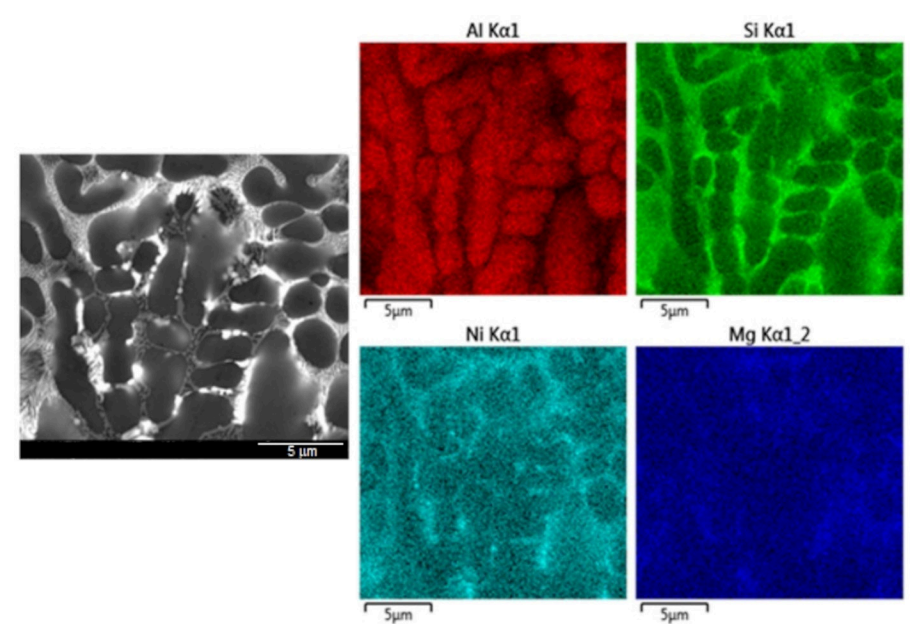
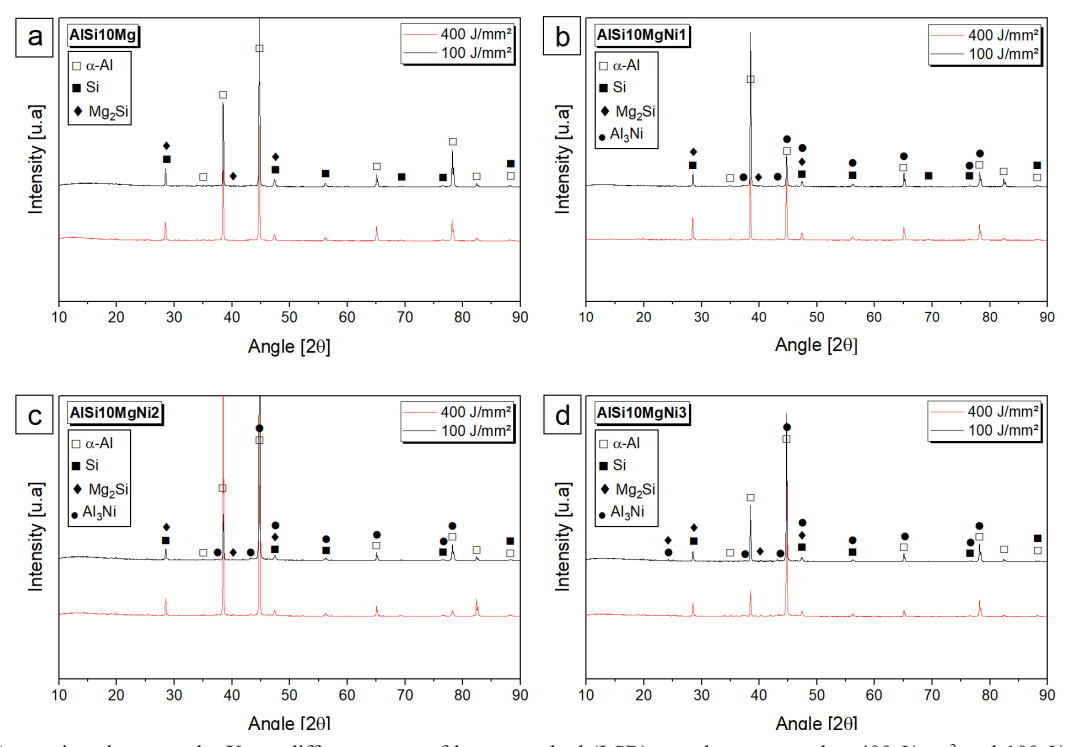


Figure 5. Typical SEM-EDS mapping of a laser remelted (LSR) AlSi10MgNi3 alloy sample processed at 400 J/mm<sup>2</sup>, including the elements Al, Si, Mg, and Ni.



**Figure 6.** Comparison between the X-ray diffractograms of laser remelted (LSR) samples processed at 400 J/mm² and 100 J/mm² for the: (a) AlSi10Mg; (b) AlSi10MgNi1; (c) AlSi10MgNi2; and (d) AlSi10MgNi3 alloys.

in the delayed precipitation of Si atoms, retaining them in the Al-rich matrix in a solid solution [46].

Experimental phase fractions were determined by SEM/BSE and Avizo 3D (Figure 7), while theoretical fractions were calculated via Thermo-Calc®. The experimental, equilibrium, and Scheil fractions were plotted together. Neither the equilibrium rule nor the Scheil model perfectly represents the experimental data, but the trends are similar: the Al<sub>2</sub>Ni fraction increases and the α-Al fraction decreases with increasing Nickel content, for both energy conditions (100 and 400 J/mm<sup>2</sup>). The extremely rapid solidification makes the Scheil model unrealistic. Surprisingly, the complete solute redistribution expected at equilibrium seems to approximate the solidification dynamics, suggesting that the partition coefficient (k<sub>0</sub>) approaches 1.0, indicating solute trapping under such extreme conditions. It is not our intention to suggest that solidification occurred under equilibrium conditions. However, assuming such a condition and extending it to a regime of complete solute trapping unexpectedly brought the model predictions into close agreement with the experimental data.

The experimentally higher Al<sub>3</sub>Ni fraction compared to equilibrium predictions may be linked to segregation during

solidification, resulting in different chemical compositions in distinct regions of the solidified part [47].

In Al–Si–Mg–Ni alloys, a Scheil simulation can predict a smaller total intermetallic fraction than equilibrium (see Figure 7) when strong solute segregation during solidification causes Ni-rich phases (e.g., Al<sub>3</sub>Ni-type) to precipitate earlier and more extensively in the primary stage. This early precipitation depletes Ni from the remaining liquid, so the terminal eutectic (normally a major source of intermetallics) forms in a smaller fraction and with a lower Ni share.

The effect becomes more pronounced during rapid solidification, as solid-state diffusion is even more limited and solidification occurs over a shorter time, leaving less opportunity for Ni to repartition into the liquid. Under these conditions, the early tie-up of Ni in primary intermetallics reduces the eutectic fraction further, making Scheil's underestimation of total intermetallics more relevant to the actual microstructure.

A nanoindentation grid was applied to a test area measuring a total of 20  $\mu m$  by 20  $\mu m$  to encompass groups of all microstructural phases. The identified clusters were related to the  $\alpha$ -Al, Al+Si, and Al+Si+Al3Ni constituents forming the

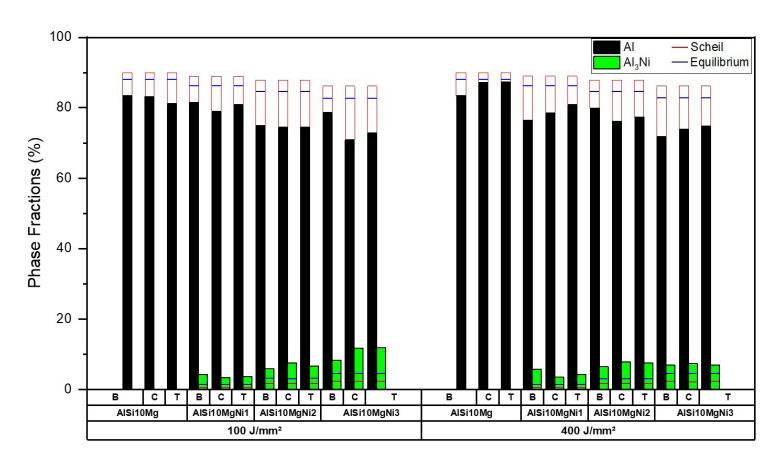


Figure 7. Phase fractions from experimental data and CALPHAD calculations in laser remelted (LSR) AlSi10MgNi(x) samples at the base (B), center (C), and top (T) of the laser-treated regions at 100 J/mm² and 400 J/mm².

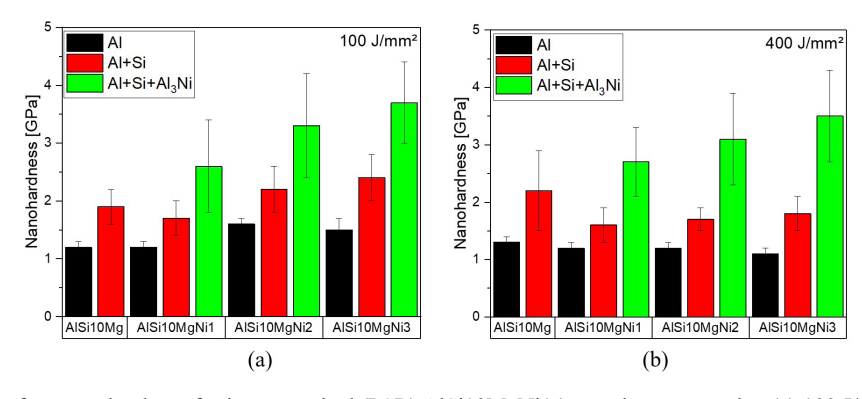


Figure 8. Comparison of average hardness for laser remelted (LSR) AlSi10MgNi(x) samples processed at (a) 100 J/mm² and (b) 400 J/mm². These results refer to the top regions of the laser-treated areas.

microstructure. Figures 8a and 8b illustrate the average hardness values of these phases after remelting with 100 J/mm² and 400 J/mm². The 0Ni alloy comprises Al-rich and Si phases. With increasing Ni content (from 1Ni to 3Ni), a third phase (Al3Ni) develops, increasing the hardness. The hardness of the Al+Si+Al3Ni group increases with Ni due to the larger fraction of Al3Ni. For Al+Si, the increase may be associated with the modification of Si particle size. The average hardness values of Al+Si are lower at 400 J/mm² due to slower solidification and formation of a coarser microstructure. However, the Al+Si+Al3Ni group exhibits relatively consistent hardness, regardless of Ni content or energy density. The energy density employed discernibly impacts the micromechanical properties of the microstructure in the laser-treated region.

The wear data of the samples do not show significant differences in terms of Ni content, spacing ( $\lambda$ ), or energy density, with similar wear volumes for all tested conditions and alloys, as can be seen in Figure 9. This is attributed to the extreme refinement of the cells formed on the surface of the laser-treated samples, as shown in Figure 2. Compared to the laser-treated samples, which showed wear volumes around 0.025 mm³, the as-cast samples exhibited values of approximately 0.035 mm³, a significantly higher amount and lower wear resistance.

# 4 Case study 2: micromorphologies and microhardness evolution in Al-(x%Mg)-0.1%Sc alloys

The LSR process was applied to substrates of Al(-3, -5, -10)% Mg-0.1% Sc (wt.%) alloys obtained by upward

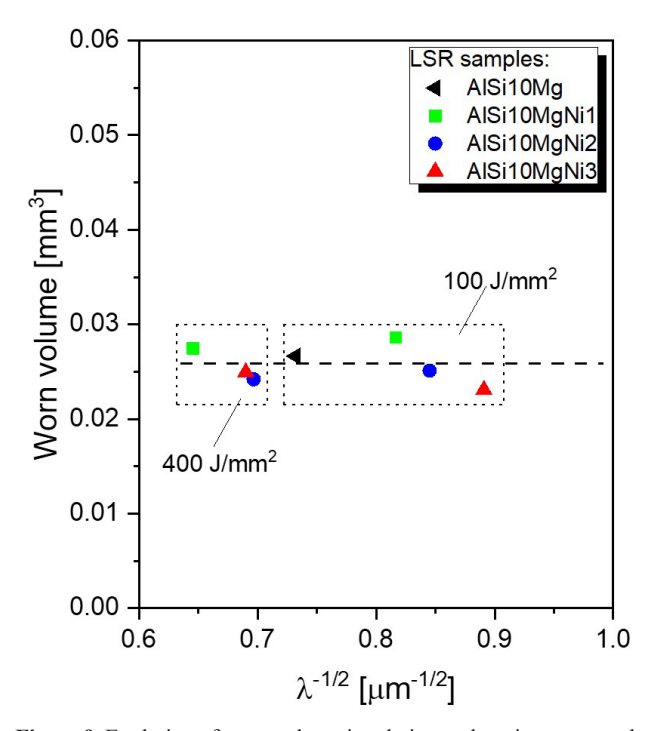


**Figure 9.** Evolution of worn volume in relation to the microstructural spacing of the AlSi10MgNi(x) samples treated by LSR.

directional solidification (DS). LSR, by imposing more severe solidification conditions than DS, results in distinct microstructures and properties. The samples for LSR, plates measuring 25 mm x 21 mm x 4 mm, were prepared from the transversal cutting of DS ingots.

For the LSR, an IPG YLR-500-MM-AC-Y14 laser was used, with a wavelength of 1070 nm and an estimated beam diameter of  $\sim\!100~\mu m$  at the focus. Prior to the process, the sample surfaces were shot-blasted with steel grit (80  $\mu m$ , 4.5 kgf/cm²) to improve laser absorption, and cleaned in an ultrasonic bath with ethyl alcohol. The LSR was performed under an argon shielding gas flow, forming isolated tracks with 2 mm separation.

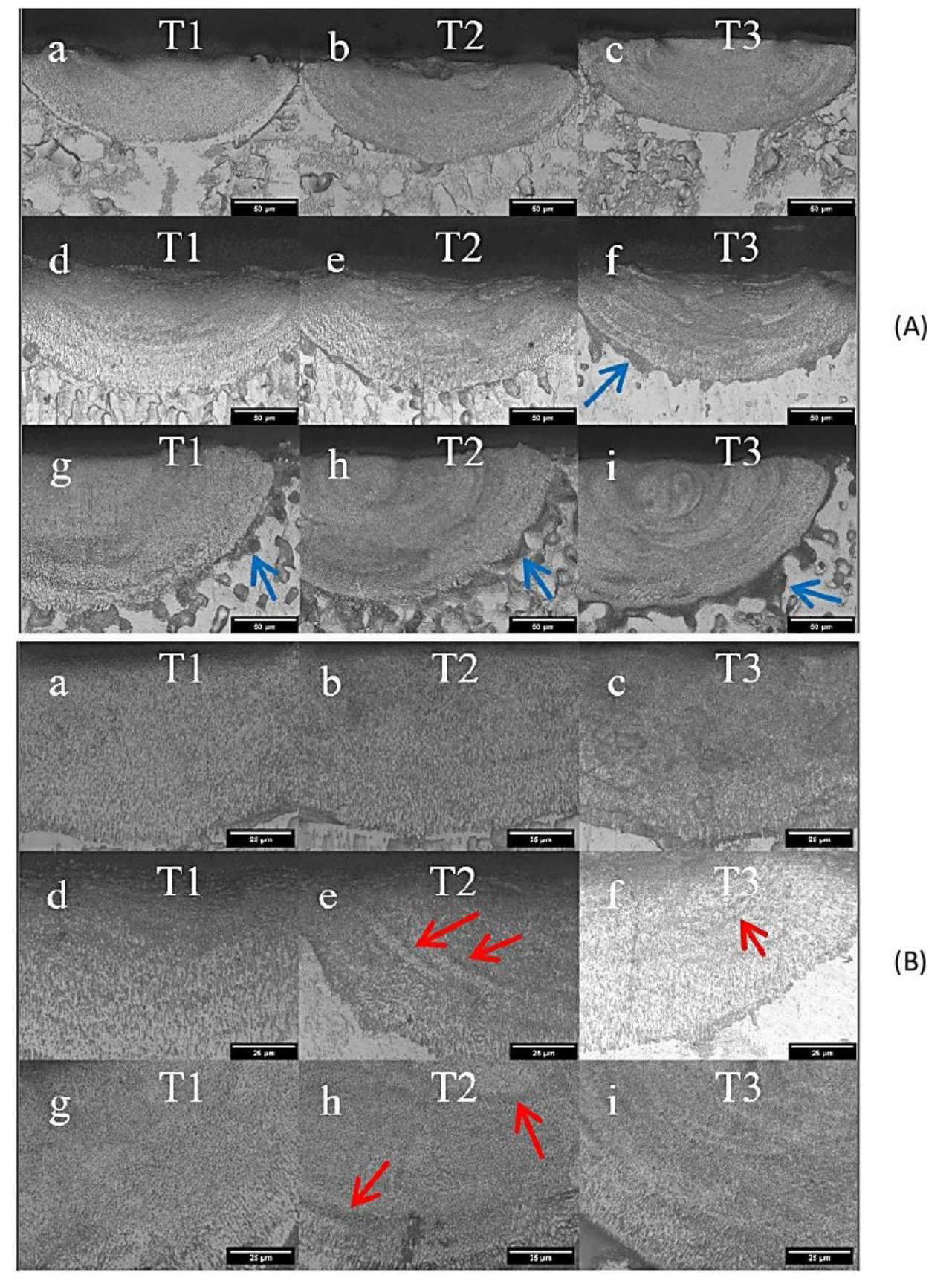
With a laser power (Q) of 250 W and scanning speeds (v) of 25, 50, and 100 mm/s, three tracks were obtained on each substrate, with corresponding energy densities of 100 (T1), 50 (T2), and 25 (T3) J/mm<sup>2</sup>, respectively.

The tracks were characterized by optical microscopy (OM), scanning electron microscopy (SEM), and Vickers microhardness. For microstructural revelation, a solution composed of HNO<sub>3</sub>, HCl, H<sub>2</sub>O, and HF was applied. An Olympus BX41M-LED optical microscope was used for observation and determination of the cellular spacing ( $\lambda_c$ ) at the base of the tracks using the intercept method. An FEI INSPECT S50 SEM was also utilized for microstructural analyses.

Vickers microhardness measurements were performed on the LSR-treated samples in both the transverse section (base region) and on the surface/top of the track. For each track, between 5 and 10 Vickers microhardness measurements were taken on both the top region of the track and its transverse section. A Shimadzu HMV-G20ST durometer was used, following the E92-17 standard. The applied loads were 0.20 kgf for 15s on the surface of the substrates and melt pools, and 0.01 kgf for 15s on the base of the transverse section of the remelted pools. Figure 10 shows the optical micrographs of the remelted regions, evidencing very refined microstructures in tracks T1, T2, and T3 of the studied A1-Mg-Sc alloys.

With increasing Mg content, an increase in the width (w) and depth (d) of the tracks was observed. For Al-3Mg-0.1Sc, w was between 226-230  $\mu m$  and d between 78-80  $\mu m$ . In Al-5Mg-0.1Sc, w ranged from 253-270  $\mu m$  and d from 87-96  $\mu m$ . For Al-10Mg-0.1Sc, w reached 291-313  $\mu m$  and d 121-125  $\mu m$ .

A notable aspect in the Al-10Mg-0.1Sc alloy is the presence of a more prominent interface (blue arrows in Figure 10A), likely a product of interfacial remelting of the substrate. This influences the growth of cells at the base of the melt pool. Consequently, the resulting melt pool tends to penetrate slightly into areas of the substrate where the liquid reaches equilibrium with the lower melting point eutectic microconstituent, as opposed to regions where equilibrium exists between the  $\alpha$ -Al (Mg) phase and the molten alloy. There appears to be an effect related to the formation of these pockets at the treated/untreated boundary, with larger



 $\label{eq:Figure 10.} Figure 10. Optical micrographs of the three tracks produced by LSR (Laser Surface Remelting) with the Al-3Mg-0.1Sc (a, b, c), Al-5Mg-0.1Sc (d, e, f), and Al-10Mg-0.1Sc (g, h, i) alloys, previously solidified at (A) 5 K/s and (B) 2 K/s. Track 1 (T1 – 100 J/mm²): Left (a, d, g); Track 2 (T2 – 50 J/mm²): Center (b, e, h); Track 3 (T3 – 25 J/mm²): Right (c, f, i) [48,49].$ 

pocket formation observed for higher Mg contents and lower energy densities.

The alloy composition affects the solid-liquid (S/L) interface formation, resulting in a very thin layer of altered eutectic products with cellular growth (Figure 10B), similar to Al-Cu alloys [50,51]. The microstructure obtained by the LSR on a substrate solidified at 2 K/s was microstructurally and dimensionally like that in the substrate at 5 K/s, with a predominance of cells and possible localized compositional fluctuations (bands) in the tracks (indicated by red arrows).

Detailed microstructural analyses of band formation in laser processing were conducted in previous studies [26,52]. These studies revealed that these compositional fluctuations consist of a sequence of light and dark bands that develop approximately parallel to the solid/liquid (S/L) interface. The dark bands have a dendritic or eutectic structure, while the light bands show no microsegregation; and are likely the result of a planar front growth morphology. Higher solidification velocities appear to trigger the growth of biphasic bands in conjunction with cellular growth under this condition. There was no defined or discernible transition between these structures.

During chemical etching, Mg was selectively removed from the interfacial and banded regions formed after LSR. This Mg removal can be observed in Figure 11, which presents SEM/BSE images of the LSR tracks on the Al-5Mg-0.1Sc alloy substrate.

With decreasing laser energy density, the occurrence of banding is accentuated, meaning it is less prominent in T1 and more pronounced in T3 (arrows). Another notable aspect of the process is the interference with phase solubility due to rapid solidification. Intermetallic Al-Fe phases (Al<sub>6</sub>Fe) are visible only in the substrate (highlighted circles), whereas in the tracks, there is no evidence of Fe-containing phases, which can be detrimental to mechanical properties.

Another microstructural aspect measured in the optical images was the cellular spacing ( $\lambda_c$ ). Table 1 presents the measurements of the cellular, intercellular, and banded fractions, and the corresponding  $\lambda_c$  at the base of the tracks

obtained by LSR of the Al-Mg-Sc alloys on substrates solidified at 2 K/s and 5 K/s. A directly proportional relationship was established between the  $\lambda_{\rm C}$  and the energy density. On average,  $\lambda_{\rm C}$  ranged from 0.97  $\mu m$  to 1.24  $\mu m$  in the tracks. Compared to the  $\lambda_{\rm C}$  of the substrates, the  $\lambda_{\rm C}$  in the tracks decreased between 16 times (in the case of T1, 5 K/s substrate, Al-3Mg-0.1Sc) and 52 times (T3, 2 K/s substrate, Al-10Mg-0.1Sc). The average intercellular fraction fluctuated between 0.24-0.27; the cellular fraction between 0.43-0.57; and the banded fraction between 0.16-0.44, suggesting an inversely proportional relationship between the cellular and banded fractions, with the intercellular fraction remaining constant.

Figure 12a demonstrates that the hardness at the top of the LSR tracks in Al-3Mg-0.1Sc and Al-5Mg-0.1Sc alloys increases with decreasing energy density.

For the microhardness at the base of the tracks (Figure 12b), concerning the cellular spacing  $(\lambda_c)$  for a 2 K/s substrate, the Al-3Mg-0.1Sc and Al-5Mg-0.1Sc alloys show an increase in microhardness with decreasing  $\lambda_c$ , which has not been observed in Al-10Mg-0.1Sc. Smaller  $\lambda_c$  values were measured for Al-3Mg-0.1Sc, with an increase in hardness.

To provide an idea of the microhardness improvement, the as-cast condition of the Al-5Mg-0.1Sc alloy yielded an average value of 75 HV, which is lower than that obtained in the remelted region of the same alloy, as shown in Figure 12(a). According to the trend indicated in Figure 12b, a decrease in  $\lambda_{\rm C}$  to critical values close to 0.75  $\mu m$  would contribute to increase the microhardness to the average levels obtained in the substrate.

Even though a lower energy density results in a smaller cellular fraction, there is a significant correlation between microhardness and  $\lambda_{\rm c}$  for the Al-3Mg-0.1Sc and Al-5Mg-0.1Sc alloys. The LSR can increase microhardness, surpassing the DS substrates. With optimized conditions, Al-10Mg-0.1Sc could reach or even exceed the substrate hardness due to favorable morphological transformations and refinement of the microstructures, that promote increased hardness, such as cellular refinement.

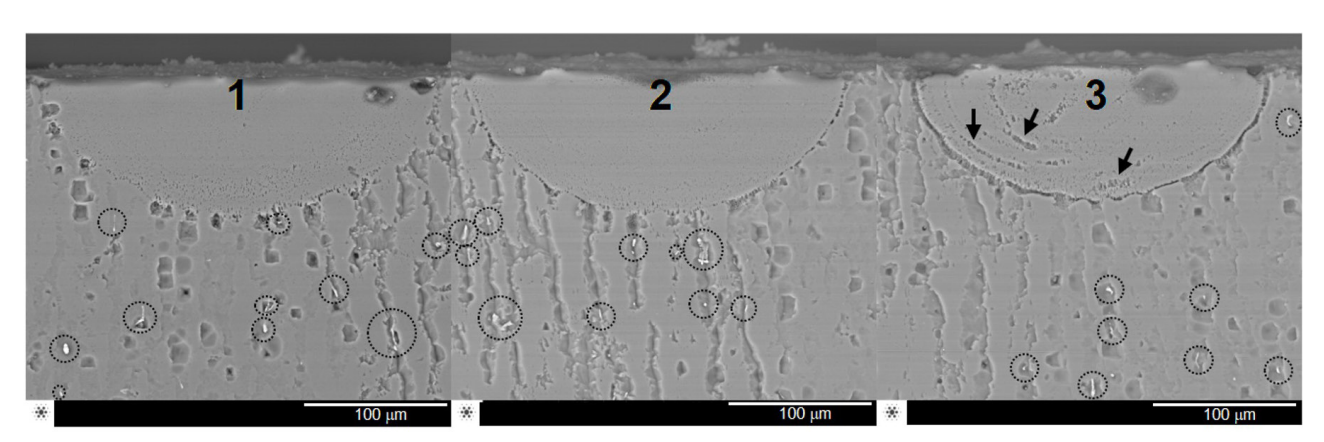


Figure 11. SEM/BSE images of the tracks 1, 2, and 3 (100, 50, and 25 J/mm<sup>2</sup>, respectively) obtained by LSR of the Al-5%Mg-0.1%Sc alloy.

Table 1. Cellular, intercellular, and banded fractions, and cellular spacings related to the tracks obtained by LSR at a laser power of 250 W on the 2 K/s solidified substrates of the studied Al-Mg-Sc alloys

Substrate/Alloy	Cooling rate of original substrate surface (K/s)	Cell spacing from the substrate surface (µm)	Condition – Energy density (J/mm²)	Cell spacing at the base of the treated region (µm)	Cell fraction	Intercellular fraction	Banded fraction
AI-3Mg-0.1Sc	2 K/s	22.3	Track 1 - 100	1.10	0.51	0.25	0.25
			Track 2 - 50	1.05	0.44	0.25	0.31
			Track 3 - 25	0.75	0.35	0.22	0.44
			Average	0.97	0.43	0.24	0.33
	5 K/s	19.1	Track 1 - 100	1.20	0.56	0.24	0.20
			Track 2 - 50	1.02	0.58	0.30	0.12
			Track 3 - 25	0.88	0.56	0.28	0.16
			Average	1.03	0.57	0.27	0.16
AI-5Mg-0.1Sc	2 K/s	29.6	Track 1 – 100	1.40	0.61	0.29	0.10
			Track 2 - 50	1.27	0.48	0.23	0.31
			Track 3 - 25	1.05	0.50	0.22	0.28
			Average	1.24	0.53	0.25	0.23
	5 K/s	19.8	Track 1 - 100	1.20	0.65	0.32	0.03
			Track 2 - 50	1.11	0.52	0.29	0.18
			Track 3 - 25	0.97	0.36	0.20	0.44
			Average	1.09	0.51	0.27	0.22
A/-10Mg-0.1Sc	2 K/s	46.5	Track 1 - 100	1.27	0.57	0.25	0.18
			Track 2 - 50	0.99	0.49	0.24	0.27
			Track 3 - 25	0.90	0.57	0.26	0.17
			Average	1.05	0.55	0.25	0.21
	5 K/s	35.4	Track 1 – 100	1.56	0.42	0.24	0.34
			Track 2 - 50	1.14	0.41	0.24	0.35
			Track 3 – 25	0.74	0.49	0.25	0.27
			Average	1.15	0.44	0.24	0.32

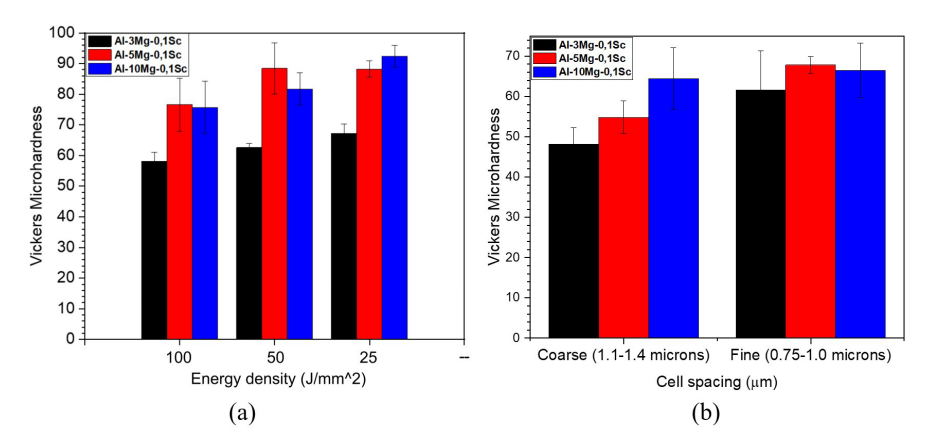


Figure 12. Vickers microhardness variations as a function of (a) energy density and (b) cellular spacing in the base of the laser-treated regions of the Al-(3, 5, and 10)%Mg-0.1%Sc alloys.

### 5 Conclusions, challenges and emerging opportunities

LSR produced highly refined cellular/dendritic microstructures (spacing from 1 to 2  $\mu$ m) in the AlSi10Mg-Ni alloys, with Ni addition increasing Al<sub>3</sub>Ni fraction and hardness, while higher cooling rates further refined phases. Wear resistance improved compared to as-cast alloys, with

all LSR-treated samples showing similar performance regardless of Ni content or energy density, owing to the uniformly fine surface layer.

LSR drastically refined cellular spacing (up to 52× smaller than substrates) in the Al-Mg-Sc alloys, with Mg content controlling melt pool dimensions and lower energy densities favoring band formation and melt pool/substrate

interfacial remelting. Microhardness increased with reduced cell size, particularly in Al-3Mg-0.1Sc and Al-5Mg-0.1Sc, surpassing as-cast values, while Al-10Mg-0.1Sc showed less direct correlation but still benefited from refined morphologies.

At least three major research from these results and development directions can be identified for LSR (Laser Surface Remelting) in Al alloys:

- a) Evaluating different morphologies of the formed intermetallics throughout the treated zone using both 2D image analysis and 3D X-ray microtomography, with the potential to determine volumetric morphological parameters. These studies can significantly enhance the understanding of solidification and surface properties in laser-treated parts.
- b) Determining micromechanical properties through nanohardness testing, and linking these results to the wear resistance of laser-treated areas.

c) Conducting LSR tests with energy densities below 25 J/mm² to explore the possibility of achieving even more refined modified microstructures.

### Acknowledgements

The authors extend their gratitude to FAPESP (grant #2023/06107-3) and CNPq. This study was partly funded by the Coordenação de Aperfeiçoamento de Pessoal de Nível Superior (CAPES) – Financing Code 001. The authors also take this opportunity to express their appreciation to Nikhilesh Chawla from Purdue University for allowing the use of the SEM and nanohardness tester, and to Profs. Piter Gargarella from UFSCar and Aline Gonçalves Capella from Unifesp for providing access to the laser equipment. Special thanks are also extended to the Structural Characterization Laboratory (LCE) at DEMa-UFSCar and PPGCEM-UFSCar.

### References

- 1 Kalita SJ. Microstructure and corrosion properties of diode laser melted friction stir weld of aluminum alloy 2024 T351. Applied Surface Science. 2011;257(9):3985-3997. http://doi.org/10.1016/j.apsusc.2010.11.163.
- 2 Richman RH, McNaughton WP. Correlation of cavitation erosion behavior with mechanical properties of metals. Wear. 1990;140(1):63-82. http://doi.org/10.1016/0043-1648(90)90122-Q.
- 3 Zhong M, Liu W. Laser surface cladding: the state of the art and challenges. Proceedings of the Institution of Mechanical Engineers. Part C, Journal of Mechanical Engineering Science. 2010;224(5):1041-1060. http://doi.org/10.1243/09544062JMES1782.
- 4 Dubourg L, Archambeault J. Technological and scientific landscape of laser cladding process in 2007. Surface and Coatings Technology. 2008;202(24):5863-5869. http://doi.org/10.1016/j.surfcoat.2008.06.122.
- 5 Singh A, Harimkar SP. Laser surface engineering of magnesium alloys: a review. Journal of the Minerals Metals & Materials Society. 2012;64(6):716-733. http://doi.org/10.1007/s11837-012-0340-2.
- 6 Steen PH, Ehrhard P, Schüssler A. Depth of melt- pool and heat- affected zone in laser surface treatments. Metallurgical and Materials Transactions. A, Physical Metallurgy and Materials Science. 1994;25(2):427-435. http://doi.org/10.1007/BF02647988.
- 7 Cheung N, Ierardi M, Garcia A, Vilar R. The use of artificial intelligence for the optimization of a laser transformation hardening process. Lasers in Engineering. 2000;10:275-291.
- 8 Kannatey-Asibu E Jr. Principles of laser materials processing. United States of America: John Wiley & Sons, Ed.; 2009.
- 9 Bi G, Chen S, Jiang J, Li Y, Chen T, Chen X-B, et al. Effects of laser surface remelting on microstructure and corrosion properties of Mg-12Dy-1.1Ni alloy. Journal of Materials Engineering and Performance. 2023;32(6):2587-2597. http://doi.org/10.1007/s11665-022-06933-y.
- 10 Ramakrishnan BP, Lei Q, Misra A, Mazumder J. Effect of laser surface remelting on the microstructure and properties of Al-Al2Cu-Si ternary eutectic alloy. Scientific Reports. 2017;7(1):13468. http://doi.org/10.1038/s41598-017-13953-5. PMid:29044169.
- 11 Kurz W, Fisher D. Fundamentals of solidification. 4th ed. Switzerland: Trans Tech Publications; 1998. http://doi.org/10.4028/www.scientific.net/RC.35.
- 12 Kuai Z, Li Z, Liu B, Liu W, Yang S. Effects of remelting on the surface morphology, microstructure and mechanical properties of AlSi10Mg alloy fabricated by selective laser melting. Materials Chemistry and Physics. 2022;285:125901. http://doi.org/10.1016/j.matchemphys.2022.125901.

- 13 Boschetto A, Bottini L, Pilone D. Effect of laser remelting on surface roughness and microstructure of AlSi10Mg selective laser melting manufactured parts. International Journal of Advanced Manufacturing Technology. 2021;113(9-10):2739-2759. http://doi.org/10.1007/s00170-021-06775-3.
- 14 Han Q, Jiao Y. Effect of heat treatment and laser surface remelting on AlSi10Mg alloy fabricated by selective laser melting. International Journal of Advanced Manufacturing Technology. 2019;102(9-12):3315-3324. http://doi.org/10.1007/s00170-018-03272-y.
- 15 Masood Arif Bukhari S, Husnain N, Arsalan Siddiqui F, Tuoqeer Anwar M, Abbas Khosa A, Imran M, et al. Effect of laser surface remelting on microstructure, mechanical properties and tribological properties of metals and alloys: a review. Optics & Laser Technology. 2023;165:109588. http://doi.org/10.1016/j.optlastec.2023.109588.
- 16 Yilbas BS, Arif AFM, Karatas C, Raza K. Laser treatment of aluminum surface: analysis of thermal stress field in the irradiated region. Journal of Materials Processing Technology. 2009;209(1):77-88. http://doi.org/10.1016/j. jmatprotec.2008.01.047.
- 17 de Moura DA, de Gouveia GL, Figueira G, Garcia A, Gargarella P, Spinelli JE. Laser remelting of AlSi10Mg(-Ni) alloy surfaces: influence of ni content and cooling rate on the microstructure. International Journal of Advanced Manufacturing Technology. 2022;120(11-12):8117-8132. http://doi.org/10.1007/s00170-022-09263-4.
- 18 Zhong M, Liu W, Zhang H. Corrosion and wear resistance characteristics of NiCr coating by laser alloying with powder feeding on grey iron liner. Wear. 2006;260(11-12):1349-1355. http://doi.org/10.1016/j.wear.2005.09.033.
- 19 Cheung N, Cruz KAS, Cante MV, Spinelli JE, Ierardi MCF, Garcia A. Numerical and experimental analysis of rapidly solidified laser remelted Al 5wt Pct Ni surfaces. International Journal of Microstructure and Materials Properties (IJMMP). 2010;5(2/3):193. http://doi.org/10.1504/IJMMP.2010.035939.
- 20 Steen WM, Mazumder J. Laser material processing. London: Springer; 2010. http://doi.org/10.1007/978-1-84996-062-5.
- 21 Liu YJ, Liu Z, Jiang Y, Wang GW, Yang Y, Zhang LC. Gradient in microstructure and mechanical property of selective laser melted AlSi10Mg. Journal of Alloys and Compounds. 2018;735:1414-1421. http://doi.org/10.1016/j. jallcom.2017.11.020.
- 22 Tomida S, Nakata K, Shibata S, Zenkouji I, Saji S. Improvement in wear resistance of hyper-eutectic Al Si cast alloy by laser surface remelting. Surface and Coatings Technology. 2003;169-170:468-471. http://doi.org/10.1016/S0257-8972(03)00100-2.
- 23 Osório WR, Cheung N, Peixoto LC, Garcia A. Corrosion resistance and mechanical properties of an Al 9wt% Si alloy treated by laser surface remelting. International Journal of Electrochemical Science. 2009;4(6):820-831. http://doi.org/10.1016/S1452-3981(23)15186-8.
- 24 Roscher M, Sun Z, Jägle EA. Designing Al alloys for laser powder bed fusion via laser surface melting: microstructure and processability of 7034 and modified 2065. Journal of Materials Processing Technology. 2024;326:118334. http://doi.org/10.1016/j.jmatprotec.2024.118334.
- 25 Gill SC, Zimmermann M, Kurz W. Laser Resolidification of the AlAl2Cu Eutectic: The Coupled Zone. Acta Metallurgica et Materialia. 1992;40(11):2895-2906. http://doi.org/10.1016/0956-7151(92)90454-M.
- 26 Zimmermann M, Carrard M, Gremaud M, Kurz W. Characterization of the banded structure in rapidly solidified Al Cu alloys. Materials Science and Engineering A. 1991;134:1278-1282. http://doi.org/10.1016/0921-5093(91)90973-Q.
- 27 Liu YL, Kang SB. Solidification and segregation of Al-Mg Alloys and influence of alloy compositionand cooling rate. Materials Science and Technology. 1997;13(4):331-336. http://doi.org/10.1179/mst.1997.13.4.331.
- 28 Zhang C, Chai L, Liu Y, Li Z, Zhang F, Li X, et al. Correlating microstructural features with improved wear and corrosion resistance of laser surface remelted A356 alloy at different scanning speeds. Materials Characterization. 2023;202:113021. http://doi.org/10.1016/j.matchar.2023.113021.
- 29 Quazi MM, Fazal MA, Haseeb ASMA, Yusof F, Masjuki HH, Arslan A. Laser-based surface modifications of aluminum and its alloys. Critical Reviews in Solid State and Material Sciences. 2016;41(2):106-131. http://doi.org/1 0.1080/10408436.2015.1076716.
- 30 Ashby MF, Easterling KE. The transformation hardening of steel surfaces by laser beams—I. Hypo-eutectoid steels. Acta Metallurgica. 1984;32(11):1935-1948. http://doi.org/10.1016/0001-6160(84)90175-5.
- 31 Liu B, Li B-Q, Li Z, Bai P, Wang Y, Kuai Z. Numerical investigation on heat transfer of multi-laser processing during selective laser melting of AlSi10Mg. Results in Physics. 2019;12:454-459. http://doi.org/10.1016/j.rinp.2018.11.075.

- 32 Cruz KS, Meza ES, Fernandes FAP, Quaresma JMV, Casteletti LC, Garcia A. Dendritic arm spacing affecting mechanical properties and wear behavior of Al-Sn and Al-Si alloys directionally solidified under unsteady-state conditions. Metallurgical and Materials Transactions. A, Physical Metallurgy and Materials Science. 2010;41(4):972-984. http://doi.org/10.1007/s11661-009-0161-2.
- 33 Kou S. Welding metallurgy. 3rd ed. United States of America: John Wiley & Sons; 2021.
- 34 Pinto MA, Cheung N, Ierardi MCF, Garcia A. Microstructural and Hardness investigation of an aluminum—copper alloy processed by laser surface melting. Materials Characterization. 2003;50(2-3):249-253. http://doi.org/10.1016/S1044-5803(03)00091-3.
- 35 Yao Z, Ren W, Allison J. Microstructure and microsegregation characterization of laser surfaced remelted Al-3wt%Cu alloys. Research Square. 2021. Preprint. http://doi.org/10.21203/rs.3.rs-1002008/v1.
- 36 Wang J, Wang H, Gao H, Yang J, Zhang M, Cheng X, et al. Crystal growth for different substrate orientations during laser directed solidification of single crystal superalloys. Journal of Alloys and Compounds. 2023;957:170219. http://doi.org/10.1016/j.jallcom.2023.170219.
- 37 Hearn W, Bogno A-A, Spinelli J, Valloton J, Henein H. Microstructure solidification maps for Al-10 Wt Pct Si alloys. Metallurgical and Materials Transactions. A, Physical Metallurgy and Materials Science. 2019;50(3):1333-1345. http://doi.org/10.1007/s11661-018-5093-2.
- 38 Hosch T, England LG, Napolitano RE. Analysis of the high growth-rate transition in Al–Si eutectic solidification. Journal of Materials Science. 2009;44(18):4892-4899. http://doi.org/10.1007/s10853-009-3747-6.
- 39 Liu Y, Luo L, Han C, Ou L, Wang J, Liu C. Effect of Fe, Si and cooling rate on the formation of Fe- and Mn-Rich Intermetallics in Al–5Mg–0.8Mn alloy. Journal of Materials Science and Technology. 2016;32(4):305-312. http://doi.org/10.1016/j.jmst.2015.10.010.
- 40 Sha M, Wu S, Wang X, Wan L, An P. Effects of cobalt content on microstructure and mechanical properties of hypereutectic Al–Si alloys. Materials Science and Engineering A. 2012;535:258-263. http://doi.org/10.1016/j.msea.2011.12.077.
- 41 Zhang W, Liu Y, Yang J, Dang J, Xu H, Du Z. Effects of Sc content on the microstructure of As-Cast Al-7wt.%. Materials Characterization. 2012;66:104-110. http://doi.org/10.1016/j.matchar.2011.11.005.
- 42 Chen X, Liu H, Zhan Y, Tang H. Microstructure optimization and mechanical properties of lightweight Al—Mg 2 Si in-Situ composite. International Journal of Materials Research. 2016;107(9):842-850. http://doi.org/10.3139/146.111405.
- 43 Canté MV, Spinelli JE, Ferreira IL, Cheung N, Garcia A. Microstructural development in Al-Ni alloys directionally solidified under unsteady-state conditions. Metallurgical and Materials Transactions. A, Physical Metallurgy and Materials Science. 2008;39(7):1712-1726. http://doi.org/10.1007/s11661-008-9536-z.
- 44 Peres MD, Siqueira CA, Garcia A. Macrostructural and microstructural development in Al–Si Alloys directionally solidified under unsteady-state conditions. Journal of Alloys and Compounds. 2004;381(1-2):168-181. http://doi.org/10.1016/j.jallcom.2004.03.107.
- 45 Gomes LF, Silva BL, Garcia A, Spinelli JE. Dendritic growth, solidification thermal parameters, and Mg content affecting the tensile properties of Al-Mg-1.5 Wt Pct Fe alloys. Metallurgical and Materials Transactions. A, Physical Metallurgy and Materials Science. 2017;48(4):1841-1855. http://doi.org/10.1007/s11661-017-3978-0.
- 46 Yang G, Fu B, Dong T, Li G. Effect of laser remelting on the microstructure and properties of the aluminum high silicon alloy coating. Journal of Materials Processing Technology. 2024;324:118278. http://doi.org/10.1016/j.jmatprotec.2023.118278.
- 47 Gomes LG. Microestrutura dendrítica, macrossegregação e microporosidade na solidificação de ligas ternárias Al-Si-Cu [tese]. Campinas: Universidade Estadual de Campinas; 2012. http://doi.org/10.47749/T/UNICAMP.2012.865887.
- 48 Nunes AT, de Gouveia GL, Riva R, Capella AG, Garcia A, Spinelli JE. Laser resolidification of Al-5Mg-0.1Sc alloy: growth of cells and banded structures. Journal of Alloys and Compounds. 2024;973:172889. http://doi.org/10.1016/j.jallcom.2023.172889.
- 49 Nunes AT, Riva R, Capella AG, Garcia A, Spinelli JE. Influence of Mg content on microstructure coarsening, molten pool size, and hardness of laser remelted Al(- x) –Mg–Sc alloys. ACS Omega. 2024;9(36):38248-38261. http://doi.org/10.1021/acsomega.4c06126. PMid:39281895.

- 50 Zweiacker KW, Liu C, Gordillo MA, McKeown JT, Campbell GH, Wiezorek JMK. Composition and automated crystal orientation mapping of rapid solidification products in hypoeutectic Al-4 at.%. Acta Materialia. 2018;145:71-83. http://doi.org/10.1016/j.actamat.2017.11.040.
- 51 Wiezorek JMK, Liu C, Farjami S, Zweiacker KW, Mckeown JT, Campbell GH. Composition and crystal orientation mapping of nano-scale multi-phase rapid solidification microstructures in hypo-eutectic Al-Cu alloy thin films. Microscopy and Microanalysis. 2017;23(S1):1078-1079. http://doi.org/10.1017/S1431927617006055.
- 52 Boettinger WJ, Shechtman D, Schaefer RJ, Biancaniello FS. The effect of rapid solidification velocity on the microstructure of Ag-Cu Alloys. Metallurgical Transactions. A, Physical Metallurgy and Materials Science. 1984;15(1):55-66. http://doi.org/10.1007/BF02644387.

Received: 19 Jun. 2025 Accepted: 18 Set. 2025

Editor-in-charge:

André Luiz Vasconcellos da Costa e Silva 📵